Model aircraft dynamics determination and control system design through analysis of experimental data

Miguel Ángel Sobrino Pozuelo
miguel.sobrino.pozuelo@tecnico.ulisboa.pt

Instituto Superior Técnico, Universidade Lisboa, Portugal

October 2022

Abstract

The commercial and military interest in Unmanned Aerial Vehicles is continuously increasing as well as the research in these types of aircraft. There is also a particular interest in the aerospace industry, to develop commercial applications for flying wings aircraft.

This work highlights flying wing advantages and drawbacks in aerodynamics and flight dynamics. After the research part, a flying wing prototype, called CP50-V0 was built in the aerospace laboratory at Instituto Superior Técnico. The prototype was built together with Alejandro Álvarez, author of the work [1].

The prototype was tested in the aerospace laboratory's wind tunnel, with the purpose of comparing the results of the aerodynamic simulations ($XFLR5$) with the experimental data. The wind tunnel tests are designed to be low-cost. The experimental data is processed and analyzed, the results are compared with the simulations done with the software $XFLR5$. Finally, a flight dynamics model is implemented in $MATLAB$ with the final purpose of designing a control system in $SIMULINK$.

Keywords: Unmanned Aerial Vehicle, Flying Wing, Wind tunnel, $XFLR5$, Stability, Control.

1. Introduction

Recently there has been a big development of small UAVs, facilitated by new manufacturing techniques such as 3D printing or CNC machining. In addition, electronic devices for navigation such as sensors, autopilots, transmitters, etc., have become smaller, more powerful, and more affordable. One important part of the design of unmanned new concept aircraft is the determination of their stability properties, which helps in the design of flight control systems. CFD software is often used, however, complementary experimental tests are needed.

Due to the low-cost nature of small UAVs, it is usual to use rough methods when tuning the flight controllers. Performing wind tunnel experiments helps to estimate the dynamic response of the UAV model to design flight controllers.

The main objective of this study is to find an efficient and comprehensive method to design flight controllers for small UAVs. Within this main goal, this work also intends to analyze what are the most important aerodynamic features in terms of control and design of low-cost wind tunnel experiments.

2. Background

To accomplish this work it was necessary to have a background in the following disciplines: aerodynamics, flight dynamic equations, stability, etc. The following sections and the provided references, summarize the required concepts.

2.1. Aerodynamics of flying wings

One of the main advantages of Flying Wings (FW) is that its lift-to-drag relation is higher. The cruise lift-to-drag ratio of Flying Wings usually increases compared to conventional aircraft. Lift in conventional fuselages is small but greatly contributes to drag. Flying Wings configurations have a higher wing surface for a given payload, diminishing wing load. For more information see [2].

According to [3], one of the main aspects when designing a flying wing is the airfoil. The main problem is that the absence of the tail makes the longitudinal trim and longitudinal stability complex. Having a tail with a large arm makes it easier to compensate the pitch moment generated by the wing. Thus, airfoils must be also designed to make easier the pitch moment trim.

Wing and airfoil design must ensure positive

Cm_0 to achieve a positive angle of attack of equilibrium. According to [4], one way is to design the airfoil with a reflex camber. However, it may cause boundary layer separation. The other alternative is to give sweep-back and twist the wing. If the wing tips are twisted with negative incidence (tip washout) they create a local positive pitch moment. Enough twist values can achieve positive Cm_0. Therefore, the solution is a trade-off between the wing and airfoil design.

2.2. Flight dynamics of flying wings

From the works [3], [5] and the article [6] some relevant conclusions can be obtained.

The absence of a tail greatly affects all stability properties of the aircraft. Longitudinal and stability modes are usually less damped so the aircraft is harder to stabilize. The absence of a horizontal stabilizer is hard to replace. A proper center of gravity position improves stability. The stability margin (distance between the neutral point and the center of gravity) for flying wings must be large enough to give good longitudinal stability but small enough to have proper longitudinal control to trim the aircraft without problems.

Lateral stability can be improved with passive methods including vertical fins at edge control surfaces and winglets that make the role of a vertical stabilizer. However, the effectiveness of vertical fins is small due to the shorter moment arm. The best solution is to include winglets at wing tips which also improve aerodynamics reducing wing-tip vortex drag. Wing design also improves lateral stability, the larger the sweep-back the better stability. Another way is to increase dihedral and wing lateral area. Moreover, in the case of propeller-driven aircraft, pusher propeller configuration improves lateral stability.

To overcome the issue of flying wing directional control, split-ailerons are used. These ailerons deflect up and down the same way creating drag but no lift.

2.3. Dynamic equations and linearization

A detailed explanation of the equations shown in this section as well as the nomenclature followed can be found in [7].

The linear approach is usually used for aircraft flight stability analysis and control design. The non-linear differential equations system is gradually linearized.

$$
\begin{aligned}
-mg\sin\theta + F_{Tx} + F_{Ax} &= m(\dot{u} - rv + qw) \\
mg\cos\theta\sin\phi + F_{Ty} + F_{Ay} &= m(\dot{v} + ru - pw) \quad (1) \\
mg\cos\theta\cos\phi + F_{Tz} + F_{Az} &= m(\dot{w} - qu + pv)
\end{aligned}
$$

$$
\begin{aligned}
L_T + L_A &= I_x\dot{p} - J_{xz}\dot{r} + (I_z - I_y)qr - J_{xz}pq \\
M_T + M_A &= I_y\dot{q} - (I_z - I_x)pr + J_{xz}(p^2 - r^2) \quad (2) \\
N_T + N_A &= I_z\dot{r} - J_{xz}\dot{p} - (I_x - I_y)pq + J_{xz}qr
\end{aligned}
$$

$$
\begin{aligned}
p &= \dot{\phi} - \dot{\psi}\sin\theta \\
q &= \dot{\theta}\cos\phi + \dot{\psi}\cos\theta\sin\phi \quad (3) \\
r &= -\dot{\theta}\sin\phi\cos\theta\cos\phi
\end{aligned}
$$

The equations above (1,2 and 3) are respectively: nonlinear linear momentum, nonlinear angular momentum and the nonlinear cinematic angular relationship equation. These equations are written in the body axis. The absolute linear velocities are (u, v, w), oriented in the direction of the body axes (x_b, y_b, z_b). The Euler angles are (ϕ, θ, ψ). The angular velocities along each body axis are (p, q, r). Finally, F stands for linear force in the body axis and (L, M, N) are the moments. T

Starting with the linearization, the variables are now a sum of a reference condition value plus a small variation (equation 4). These new variables are called incremental variables.

$$
\begin{aligned}
u &= u_s + \Delta u & p &= p_s + \Delta p & \psi &= \psi_s + \Delta\psi \\
v &= v_s + \Delta v & q &= q_s + \Delta q & \theta &= \theta_s + \Delta\theta \quad (4) \\
w &= w_s + \Delta w & r &= r_s + \Delta r & \phi &= \phi_s + \Delta\phi
\end{aligned}
$$

The same procedure in equation 4 is applied to the aero-propulsive forces and moments.

The equations are simplified by replacing the incremental variables in the equations (1,2 and 3). Small terms are also neglected and the following flight reference condition (equation 5) is applied. The simplified equations are (6,7 and 8).

$$
\begin{aligned}
p_s = q_s = r_s = 0 &\rightarrow \dot{\phi}_s = \dot{\theta}_s = \dot{\psi}_s = 0 \\
v_s = 0 &\rightarrow \beta_s = 0 \quad (5) \\
\phi_s &= 0
\end{aligned}
$$

$$
\begin{aligned}
-mg\cos\theta_s\Delta\theta + \Delta F_X &= m(\Delta\dot{u} + w_s\Delta q) \\
mg\cos\theta_s\Delta\phi + \Delta F_Y &= m(\Delta\dot{v} + u_s\Delta r - w_s\Delta p) \\
-mg\sin\theta_s\Delta\theta + \Delta F_Z &= m(\Delta\dot{w} - u_s\Delta q)
\end{aligned}
$$
$$(6)$$

As can be seen, the equations (6,7, and 8) do not contain reference force and moment values. The reference values in the left term counteract the ones in the right term because the reference states are in equilibrium. The remaining equation terms describe the perturbation movement, see [8] for further information about the perturbation theory.

$$
\begin{aligned}
\Delta L &= I_x\Delta\dot{p} - J_{xz}\Delta\dot{r} \\
\Delta M &= I_y\Delta\dot{q} \quad (7) \\
\Delta N &= I_z\Delta\dot{r} - J_{xz}\Delta\dot{p}
\end{aligned}
$$

$$
\begin{aligned}
\Delta p &= \Delta\dot{\phi} - \Delta\dot{\psi}\sin\theta_s \\
\Delta q &= \Delta\dot{\theta} \quad (8) \\
\Delta r &= \cos\theta_s\Delta\dot{\psi}
\end{aligned}
$$

The propulsive and aerodynamic forces must be linearized as well (equation 9). Following Bryan's work see [7], the non-steady nature of these forces can be modeled as follows:

$$\Delta X = X_u \Delta u + X_{\dot u} \Delta \dot u$$
$$\left\{ \begin{array}{l} X_u = \left(\dfrac{\partial X}{\partial u} \right)_s \\[2mm] X_{\dot u} = \left(\dfrac{\partial X}{\partial \dot u} \right)_s \end{array} \right\} \tag{9}$$

In the equation 9, for each aero-propulsive force, there are derivatives with respect to every single flight variable, these derivatives are called stability derivatives.

There are two segregated movements in aircraft flight dynamics: longitudinal and lateral-directional. The flight variables of each movement are respectively shown in equation (10).

$$\Delta X, \Delta Z, \Delta M =$$
$$f(\Delta u, \Delta w, \Delta q, \Delta \dot u, \Delta \dot w, \Delta \dot q, \Delta \delta_e, \Delta \dot \delta_e)$$
$$\Delta Y, \Delta L, \Delta N =$$
$$f(\Delta v, \Delta p, \Delta r, \Delta \dot v, \Delta \dot p, \Delta \dot q, \Delta \delta_a, \Delta \dot \delta_a, \Delta \delta_r, \Delta \dot \delta_r) \tag{10}$$

The effect of longitudinal variables is neglected on the lateral-directional movement and vice-versa. Thus, longitudinal forces derivatives with respect to lateral variables do not appear in the equations and the same for lateral forces with respect to longitudinal variables. The following derivatives are usually small and also neglected:

$$X_q, X_{\dot w}, X_{\delta_e}, Y_{\delta_a}, Y_{\dot \delta_a}, Y_{\dot \delta_r}, Z_{\dot \delta_e}, L_{\dot \delta_r}, N_{\dot \delta_a} \tag{11}$$

Hereafter, the stability derivatives presented in the equation 12, are usually selected to model the linearized areo-propulsive forces and moments. These derivatives are the most relevant ones in most practical cases. Replacing these terms in the equations 6 and 7 the system's linearization is completed.

$$\Delta X = X_u \Delta u + X_w \Delta w + X_{\delta_e} \Delta \delta_e$$
$$\Delta Y = Y_v \Delta v + Y_p \Delta p + Y_r \Delta r + Y_{\delta_r} \Delta \delta_r$$
$$\Delta Z = Z_u \Delta u + Z_w \Delta w + Z_q \Delta q$$
$$\qquad\qquad + Z_{\dot w} \Delta \dot w + Z_{\delta_e} \Delta \delta_e$$
$$\Delta L = L_v \Delta v + L_p \Delta p + L_r \Delta r + L_{\delta_a} \Delta \delta_a +$$
$$\qquad\qquad L_{\dot \delta_a} \Delta \dot \delta_a + L_{\delta_r} \Delta \delta_r \tag{12}$$
$$\Delta M = M_u \Delta u + M_w \Delta w + M_q \Delta q + M_{\dot w} \Delta \dot w$$
$$\qquad\qquad + M_{\delta_e} \Delta \delta_e + M_{\dot \delta_e} \Delta \dot \delta_e$$
$$\Delta N = N_v \Delta v + N_p \Delta p + N_r \Delta r + N_{\delta_a} \Delta \delta_a$$
$$\qquad\qquad + N_{\dot \delta_a} \Delta \dot \delta_a + N_{\delta_r} \Delta \delta_r$$

In equation 12 there are also stability derivatives with respect to control surfaces ($\delta_e, \delta_a, \delta_r, \delta_t$).

It is usual to study the dynamic system by removing dimensions and using stability derivative coefficients. First, the reference magnitudes are selected by convention i.e (mass, velocity, time, force, moment, etc.). Secondly, each term of the equation is divided by the proper reference magnitudes. This process is presented in detail in [7]. The adimensional system of equations for the longitudinal movement is described in the equation 13.

$$(2\mu D - C_{X\hat u} + 2C_{Zs} \tan \theta_s) \Delta \hat u -$$
$$\qquad C_{X\alpha} \Delta \alpha - C_{Zs} \Delta \theta = C_{X\delta_e} \Delta \delta_e$$
$$- (C_{Z\hat u} + 2C_{Zs}) \Delta \hat u + ((2\mu - C_{Z\hat{\dot\alpha}}) D - C_{Z\alpha}) \Delta \alpha -$$
$$\qquad ((2\mu + C_{Z\hat q}) D + C_{Zs} \tan \theta) \Delta \theta = C_{Z\delta_e} \Delta \delta_e$$
$$- C_{m\hat u} \Delta \hat u - (C_{m\hat{\dot\alpha}} D + C_{m\alpha}) \Delta \alpha +$$
$$\qquad (\hat I_y D^2 - C_{m\hat q} D) \Delta \theta = (C_{m\hat\delta_e} D + C_{m\delta_e}) \Delta \delta_e$$
$$D\Delta \theta = \Delta \hat q \tag{13}$$

$$Z_s + mg \cos \theta_s = 0 \quad \rightarrow \quad C_{Zs} = -\frac{mg \cos \theta_s}{1/2 \rho u_s^2 S}$$
$$X_s - mg \sin \theta_s = 0 \rightarrow$$
$$\qquad C_{Xs} = \frac{mg \sin \theta_s}{1/2 \rho u_s^2 S} = -C_{Zs} \tan \theta_s$$

The dimensionless system of equations for lateral movement is described in the equation 14.

$$(2\mu D - C_{Y\beta}) \Delta \beta - C_{Y\hat p} \Delta \hat p +$$
$$\qquad (2\mu - C_{Y\hat r}) \Delta \hat r + C_{Zs} \Delta \phi = C_{Y\delta_r} \Delta \delta_r$$
$$- C_{l\beta} \Delta \beta + (\hat I_x D - C_{l\hat p}) \Delta \hat p - (\hat J_{xz} D + C_{l\hat r}) \Delta \hat r =$$
$$\qquad (C_{l\hat\delta_a} D + C_{l\delta_a}) \Delta \delta_a + C_{l\delta_r} \Delta \delta_r \tag{14}$$
$$- C_{n\beta} \Delta \beta - (\hat J_{xz} D + C_{n\hat p}) \Delta \hat p + (\hat I_z D - C_{n\hat r}) \Delta \hat r$$
$$\qquad = C_{n\delta_a} \Delta \delta_a + (C_{n\hat\delta_r} D + C_{n\delta_r}) \Delta \delta_r$$
$$\Delta \phi = \Delta \hat p + \tan \theta_s \Delta \hat r$$
$$D\Delta \psi = \sec \theta_s \Delta \hat r$$

To determine the aircraft's stability properties the eigenvalues of the previous system of equations are calculated.

2.4. Control

In this study, the flight control system is designed and implemented with the classical control theory. This theory is based on open/closed-loop feedback. The classical control theory uses tools such as root-locus plots, Nyquist and Bode diagrams, stability criteria, etc. Most of these tools use the frequency domain analysis technique. All classical analysis tools are based on the system's transfer function,

which is the result of applying the Laplace Transform to the system of differential equation.

The controllers implemented in $SIMULINK$ are based on the Proportional Integral Derivative (PID) controller, which is the most cost-effective control technique, because of its robustness and lack of complexity. [9]

2.5. Control-oriented dynamic equations

As it is very expensive to characterize all stability derivatives by wind tunnel experiments, it is interesting to find which derivatives are more relevant for the control design. Control corrections are fast compared with the modal response of the aircraft, especially compared with Phugoid and spiral modes. In this context, some simplifications in the system of equations 13 can be done for longitudinal movement and short time responses $\Delta u \approx 0$, resulting in 15:

$$((2\mu - C_{Z\hat{\alpha}})D - C_{Z\alpha})\Delta\alpha -$$
$$(2\mu + C_{Z\hat{q}})D\Delta\theta = C_{Z\delta_e}\Delta\delta_e \quad (15)$$

$$-(C_{m\hat{\alpha}}D + C_{m\alpha})\Delta\alpha + (\hat{I}_yD^2 - C_{m\hat{q}}D)\Delta\theta$$
$$= (C_{m\hat{\delta}_e}D + C_{m\delta_e})\Delta\delta_e$$

One can see how the force balance along the X axis is no longer important together with variable Δu. This makes all Cx stability derivatives and Cz_u, Cm_u not really important for control design.

Equation 16 describes the simplified lateral movement system of equations:

$$(2\mu D - C_{Y\beta})\Delta\beta + (2\mu - C_{Y\hat{r}})\Delta\hat{r} = 0$$
$$-C_{n\beta}\Delta\beta + (\hat{I}_zD - C_{n\hat{r}})\Delta\hat{r} = C_{n\delta_r}\Delta\delta_r \quad (16)$$

The equations show that the main derivatives in this context are $(Cn_\beta, Cn_r, Cn_{\delta_r})$.

3. Implementation

This section describes how the different parts of this work are planned and accomplished. The selected aircraft configuration is a flying wing. A commercial off-the-self model is selected.

3.1. Prototype selection and manufacturing

The prototype is selected mainly due to its manufacturing simplicity and dimensions. The selected model is the Zyklon 400, its geometrical details can be found in [10]. The selected airfoil is the Eppler 186, which is a good profile for flying wings as it has a slight reflex camber to give positive C_{m0}.

Max thickness and position	10.2%, 29%
Max camber and position	0.8%, 29%
Root chord (c_{root})	275mm
Tip chord (c_{tip})	150mm

Table 1: Eppler186 airfoil details

The prototype manufacturing was done in collaboration with Alejandro Álvarez [1] and starts by cutting the wing shape. The wing was made of Styrofoam (XPS). Each semi-wing was manufactured separately. To build the semi-wing with the correct airfoil shape, wood templates were used. The airfoil details can be seen in table 1. Secondly, The wing's trailing edge was cut to detach the elevons of the semi-wings. Subsequently, the electronics bay was cut out using a cutter and then both semi-wings were glued with a plastic gun. The wing's geometrical properties are described in table 2.

Wing surface (S)	0.202m^2
Wingspan (b)	950mm
MAC ($\bar{c}$)	219mm
Tapper ratio (λ)	0.545
aspect ratio (A.R)	4.468
Sweep (Λ)	19.56°
Dihedral (Γ)	0°
Twist (θ)	0°

Table 2: Wing properties

Figure 1: CP50-V0 prototype

After that, the holes for the servo-actuators were made by melting the foam with the heat of a welder for electronics. The next step was to attach the elevons to the semi-wings with two plastic hinges each. Finally, the winglets were cut from foam blocks and they are plastic-glued to the wing tips. The completed prototype is depicted in Figure 1

3.2. Prototype modelling in $XFLR5$

The first step is to load the airfoil shape (table 1) and calculate its aerodynamic properties for different Reynold numbers and angles of attack. It is important to include in the definition of the airfoil a flap to calculate the control stability derivatives further on. The second step is to create the wing according to table 2 and choose the panel distribution (table 3). Some of the aerodynamic properties,

such as the moment coefficients depend on the center of gravity location. It is not possible to know the mass configuration ad-hoc. Thus, ror the first studies, the mass properties were estimated with the mass of the components and $XFRL5$ wing mass and inertia calculations.

Part	Main wing	Winglets
X number	20	20
X distribution	Cosine	Cosine
Y number	20	10
Y distribution	Uniform	Uniform

Table 3: XFRL5 panel distribution

Afterward, the aerodynamic analysis was set up , considering the 3D panel method and viscosity effects. The $XFRL5$ model of the prototype can be seen in Figure 2.
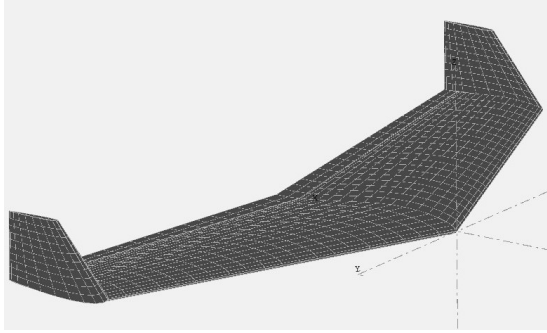
Figure 2: CP50-V0 modeled in $XFRL5$

3.3. Gravity center and inertia tests implementation

The center of gravity tests were conducted following João's work [11], the equipment used is the same one. The test device consists of two load cells mounted over an aluminum beam. The load cells were connected to an Arduino that calculates the mass over each load cell after being calibrated with a 200g mass.

$$X_{CG} = \frac{F2(Y1 + AB) + F1(Y1)}{F1 + F2} \quad (17)$$

In equation 17, F1 and F2 stand for the weight readings of each load cell 1 and 2. AB is the linear distance between the two load cells and Y1 is the distance between a reference point of the prototype and load cell 1. The result is the distance between the selected reference point and the center of gravity of the model. In the experiment, the selected reference point is the nose of the prototype.

Additionally, to correctly simulate the UAV dynamics it is important to estimate inertia moments. Firstly, an experiment was conducted. The UAV is placed over a metallic frame that was hanging from two ropes like a pendulum. Then, the model was perturbed to induce oscillations. The oscillatory period was measured with and without placing the model and after some mathematical operations [11], the inertia momentum was obtained.

3.4. Wind tunnel test design and implementation

Static and dynamic wind tunnel tests were carried out. For both experiments, the same test rig, with minor modifications, was used. The test rig consists of an aluminum frame, fixed to the wind-tunnel floor. On top of the rig, facing the air stream, a load cell assembly was mounted. The load cell device was a commercial product, the Tyto Robotics Series 1580 Test stand. These load cells allowed for measuring the aerodynamic forces, especially important for static tests.

For the static experiments, the prototype was attached to a servo actuator which in turn was fixed to the test rig. The actuator changes the angle of attack during the experiments. In addition, for each dynamic experiment, different 3D printed coupling parts were designed and manufactured to allow each degree of freedom.

For the pitch dynamic experiments, the model was attached by a shaft mounted through the coupling part's flanges. For the second dynamic experiment, a bearing was placed in a manufactured mounting plate that was attached to the model.

The dynamic experiments did not completely determine the stability, but according to equations 15 and 16, the most important stability derivatives could be estimated.

The single degree of freedom equation 18 is pitch, assuming $(C_{m\dot{\delta}_e} = 0)$.

$$\Delta\theta = \Delta\alpha$$
$$\hat{I}_y D^2 \Delta\theta - (C_{m\hat{q}} + C_{m\hat{\alpha}})D\Delta\theta = C_{m\delta_e}\Delta\delta_e \quad (18)$$

For lateral stability properties determination, the dynamic expression is the equation 19, where yaw is the only degree of freedom, assuming $(C_{n\hat{\delta}_r} = 0)$.

$$\Delta\psi = -\Delta\beta$$
$$(\hat{I}_z D^2 - C_{n\hat{r}}D + C_{n\beta})\Delta\psi = C_{n\delta_r}\Delta\delta_r \quad (19)$$

In both experiments, an Inertial Measurement Unit, (IMU) sensor was used to estimate the Euler angles. The IMU measures acceleration and angular velocity but using a state estimator with an Extended Kalman Filter it was possible to estimate the Euler angles. The IMU model is the 10 DOF IMU by WaveShare.

3.5. $SIMULINK$ flight dynamics model and control system implementation

To simulate a wide range of flight conditions and test the designed controllers, a slightly more complex model than the previous linearized one is

needed.

The Simulink block architecture is composed of three interconnected block functions. One block computes all external forces and moments, based on the instantaneous state vector (equation 20), and input vector, (equation 21). Another block computes the wind velocity depending on altitude and airspeed. Finally, the dynamics block is provided with force, moment, and wind data to compute the state's derivative vector, and finally, the state vector (equation 20) is integrated in time using the standard $SIMULINK$ explicit integration schemes.

$$x = \{p_n, p_e, p_d, u, v, w, \phi, \theta, \psi, p, q, r\} \qquad (20)$$

(p_n, p_e, p_d) is the spacial position in the inertial axis, north, east, and down, respectively. (u, v, w) are the inertial velocities components expressed in body axis, (ϕ, θ, ψ) are the Euler angles and finally (p, q, r) are the angular velocity components in body axis.

$$\delta = \{\delta_e, \delta_a, \delta_r, \delta_t\} \qquad (21)$$

The elements of δ vector (equation 21) are elevator, aileron, rudder (if applicable) and throttle inputs respectively.

The referred dynamics block implements equations 1, 2, and 3. The aero-propulsive block combines a linearized aerodynamic model, based on $XFRL5$'s lift, drag, and stability derivatives predictions with a propulsive model based on Bernoulli's principle (see [12], [13]).

3.6. $SIMULINK$ autopilot implementation
The implemented control solution is a low-level autopilot, which is capable to hold the flight variables in a determined status. The autopilot is divided into two: the lateral controller, which is able to hold the desired course angle by commanding ailerons, and the longitudinal controller, which combines three modes to hold altitude, pitch angle, or airspeed.

Both controllers are based on a hierarchical structure using the successive loop closure method, [13], as ilustrated in figure 3. An inner loop controls dynamics i.e. bank angle, and pitch angle, by actuating ailerons and elevators. Subsequently, an outer loop controls the flight variables, i.e. course angle, flight path, and airspeed.
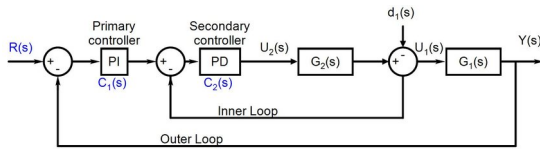

Figure 3: Successive loop closure scheme

Each loop is controlled by a PID structure. The inner loop that commands ailerons to achieve a determined bank angle has three gains (proportional, integrative, and derivative). The outer loop that controls the course is a Proportional Integral (PI) controller, which only has proportional and integrative gains.

For the longitudinal autopilot. The inner loop for pitch control is a PID controller and the outer loop for altitude control is a PI controller. In the case of airspeed hold mode, the inner loop is the same and the outer loop is also a PI controller.

4. Results
In this section, the results of simulations and experiments are described as well as the selected controller gains for the proposed control structure.

4.1. $XFLR5$ results
The winglets are modeled with a NACA 0010 airfoil. The winglet root chord is 150 mm and the tip chord is 75 mm. The winglets are placed vertically (90 degrees of dihedral) and they have a height or winglet span of 75 mm.

C_{L0}	-0.05
$C_{L\alpha}$	4.099
C_{m0}	0.054
$C_{m\alpha}$	-0.609

Table 4: $C_L(\alpha)$ and $C_m(\alpha)$ curves

In Table 4, lift coefficient for $\alpha = 0$ (C_{L0}), lift curve slope ($C_{L\alpha}$), pitch moment coefficient for $\alpha = 0$ (C_{m0}) and pitch moment coefficient slope ($C_{m\alpha}$), are described. The model is stable because the pitch moment derivative with respect to alpha is negative. Lift is negative for 0 degrees of angle of attack due to the reflex camber of the Eppler airfoil. The angle of attack of equilibrium is 5 degrees. As the final weight of the prototype is over 3.31N, the stall speed is over 7.5 m/s. To achieve C_{Lmax} it is necessary to change the elevator position from neutral to a few degrees up. With elevators in a neutral position, the cruise airspeed to achieve steady flight is 9.4 m/s. In these conditions, the minimum thrust needed is 0.242N.

The results in Table 4 are independent of the Reynolds number (they do not vary with velocity) because the potential aerodynamic theory used, thus no viscosity effects are accounted for, [14]. $XFRL5$ drag estimations can be seen in Figure 6.

As discussed before, $XFRL5$ is able to calculate most of the stability derivatives and the stability modes. In Table 5 the modal properties of the prototype with winglets, CP50 (W), and without them, are compared with other similar flying wing designs (from [3] and [15]).

Model	Phugoid	Short Period
CP50(W)	$-0.032 \pm 1.34i$	-17.33 ± 22.51
CP50	$-0.038 \pm 1.11i$	$-20.78 \pm 27.47i$
[3]	$-0.03 \pm 0.38i$	$-27.6 \pm 58i$
[15]	$-0.029 \pm 1.02i$	$-19.78 \pm 17.39i$
Model	Dutch Roll	Spiral
CP50(W)	$-0.445 \pm 5.73i$	$+0.084 \pm 0i$
CP50	$+0.013 \pm 3.62i$	$+0.102 \pm 0i$
[3]	-0.6 ± 8.2	unstable
[15]	$-0.327 \pm 3.61i$	$+0.065 \pm 0i$

Table 5: Modal comparison with other works

Table 5 shows that the flight dynamic modes are very similar for the three models. The analysis suggests that the weight, inertia, wing shape, and wing dimensions are properly balanced compared to similar flying wings in its category. The exception is the prototype without winglets, its longitudinal modes are similar to the rest although the Dutch Roll mode is one order of magnitude less damped and spiral mode is more unstable.

In general, the dynamic behavior is good expect for the prototype without winglets. Only the spiral mode is divergent but indeed it is usually unstable. As can be seen, winglets effects on lateral modes are crucial. In addition, by giving 5 degrees of dihedral angle to the wing, the spiral mode becomes less unstable. Its time to double moves from 8.25 s to 17.77 s.

4.2. **Experimental results**

The results of the center of gravity and inertia moment determination are shown in Table 6.

m_{total}	333.8 g
x_{cg}	113 mm
I_{xx}	0.009 kgm^2
I_{yy}	0.002 kgm^2
I_{zz}	0.012 kgm^2
I_{xz}	3e-5 kgm^2

Table 6: Mass properties of the prototype

Due to the small weight of the UAV and the large difference in weight with the metallic structure, there is not enough precision to notice any change in the period of the oscillations. Provided that measuring the inertia moments with the tools available in the laboratory is not possible, the inertia moments are estimated with $XFRL5$ and $CATIA$ software.

The wind tunnel stand must be attached to the prototype in the same position as the center of gravity so the pitch and yaw rotations are the same of those in free flight. In that case, the equations 18 and 19 can be used for the dynamic experiment analysis.
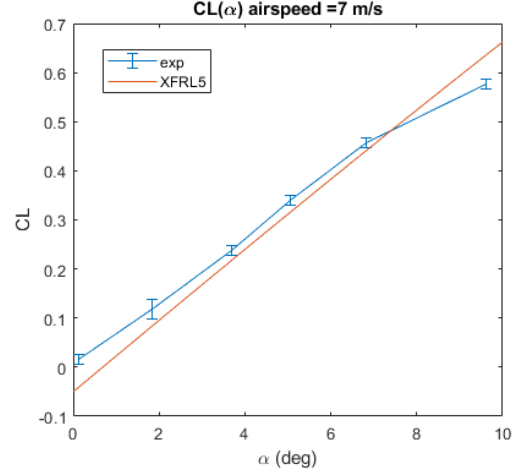

Figure 4: $C_L(\alpha)$ curve comparison (7 m/s)

Regarding the lift coefficient, $XFLR5$ estimations are really good for the airspeed of 7 m/s (Figure 4). $XFLR5$ underestimates the lift coefficient at a low angle of attack, however, it overestimates the lift coefficient slope. Unlike XFLR5, the experiment results indicate positive CL_0. The most probable reason is related to manufacturing inaccuracies. In $XFLR5$, the elevon position is perfectly neutral, however, in the real model, the position is not perfectly neutral. Another source of inaccuracy is the IMU, which has a certain bias error in the angle of attack, that may cause the lift curve to move horizontally.
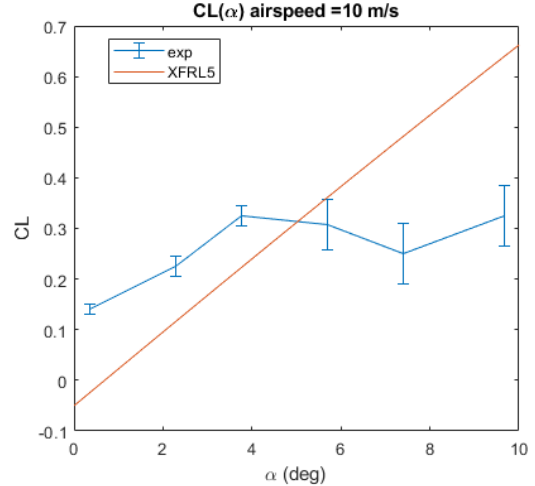

Figure 5: $C_L(\alpha)$ curve comparison (7 m/s)

Regarding the experiments for the airspeeds of 9 and 10 m/s, the experimental results are not as expected and cannot be used to perform a critical analysis. At higher airspeeds, the assembly tends to vibrate because of its poor stiffness, these vibrations cause erroneous data (see Figure 5).

In figure 6 it can be seen that $XFLR5$ underestimates drag. Real drag doubles $XFLR5$ prediction. $XFLR5$ interpolates the 2D drag calculated with XFOIL to the 3D case, this drastic approximation causes the differences. However, the order of magnitude and the behavior with the angle of attack are similar.
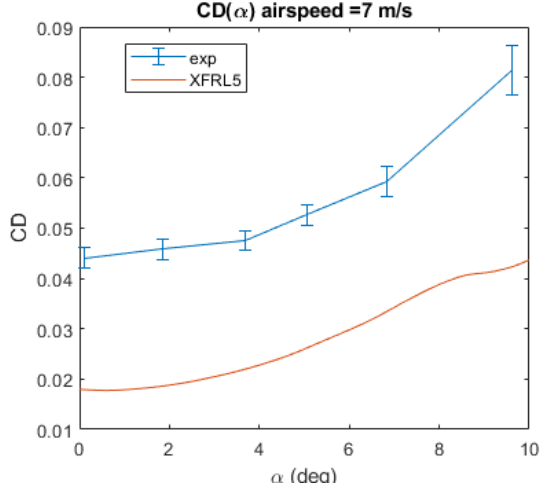

Figure 6: $C_D(\alpha)$ curve comparison (7 m/s)

It is worth to note that when airspeed changes, especially at low speeds, Reynolds number variations greatly affect boundary layer physics thus, the drag coefficient changes under these conditions, [4].

Starting with the lateral dynamic experiment, the model is mounted such that only yaw is allowed. During the experiments, the prototype is perturbed and the yaw angle, measured by the IMU, is recorded. The experiments are conducted for various airspeeds.
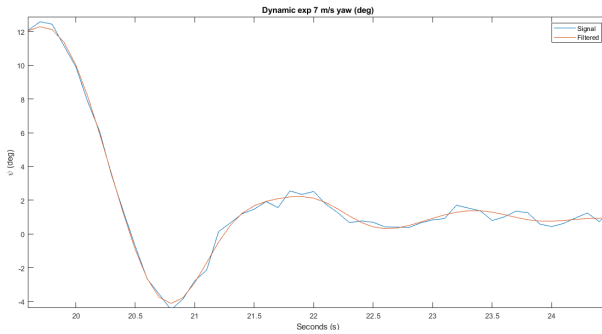

Figure 7: Response to yaw perturbation V = 7 m/s.

One can notice from Figures 7 that the response is oscillatory and under-damped. The data processed by the EKF contains noise. To remove it, a low pass filter is used to remove noise above 1Hz of bandwidth. Once the natural frequency and damping are calculated from the plots, applying the equation 19, the stability derivatives are obtained.

In general, the estimations of the stability derivatives are in the same order of magnitude as the $XFLR5$ approximation, as shown in table 7, for an airspeed of 9 m/s. In particular, $C_{n\beta}$ is close in both tests, however, the experiment suggests a value of $C_{n\hat{r}}$ three to four times higher than $XFLR5$ predictions. The comparison is done for an airspeed of 9 m/s because that is the trim airspeed for which stability derivatives are calculated in $XFRL5$.

Test	exp $C_{n\beta}$	$C_{n\beta}$	exp $C_{n\hat{r}}$	$C_{n\hat{r}}$
1	0.0275	0.0234	-0.0373	-0.01140
2	0.0265	0.0234	-0.0550	-0.01140

Table 7: Response analysis $V = 9$ m/s.

The longitudinal experiments prove that the model is stable. When airspeed raises, the prototype reaches the angle of attack of equilibrium.

The longitudinal experiment results are not easy to analyze, against all expectations the dynamic behavior is exponential, and no oscillations are observed. Looking at the equations it may be due to the effect of $C_{m\dot{\alpha}}$, whose influence can be important because the prototype inertia is in the same order of magnitude as the surrounding air inertia. It seems that the short period mode is highly damped so it is difficult to identify oscillations in the recorded noisy measures.

Figure 8: Prototype being tested in the wind tunnel

4.3. Control system design and results

The autopilot's gains design starts by linearizing the $SIMULINK$ model at the trim point. Afterward, the ailerons to bank angle and the elevator to pitch angle transfer functions are obtained.
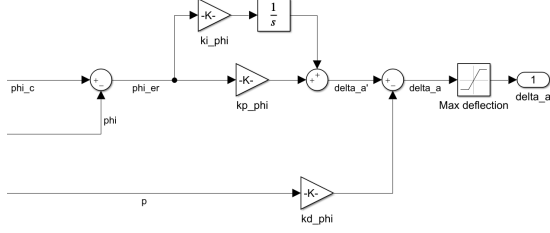
Figure 9: Bank angle inner loop

In the Figure 9, the inner loop structure for the bank angle control is depicted. The structure is equal in the case of the inner loop for pitch control.

Secondly, various simulations are done modifying the controller's gains to achieve the desired response. However, the UAV's control surfaces have certain physical limits such as the angular rate of deflection or the maximum deflection. In this case, to limit the aileron deflection, a saturation block is included.

Actuator saturation must be considered when designing the gains. Provided that the system is stable, the maximum error occurs after the command when the integral and derivative errors are zero. Once the maximum expected error is selected, the equation 22 sets an upper limit for the proportional gain to avoid saturation.

$$\delta = k_p e_{max} \quad (k_p)_{max} = \frac{\delta_{max}}{e_{max}} \quad (22)$$

After testing different gain combinations it is observed that: k_p increases the response speed but also increases oscillations and overshoot, k_d reduces overshoot but increases secondary oscillations, and k_i removes the stationary error but increases overshoot and oscillations. In addition, the lower the k_p, the bigger the static gain of the loop (stationary error) and the smaller the bandwidth.
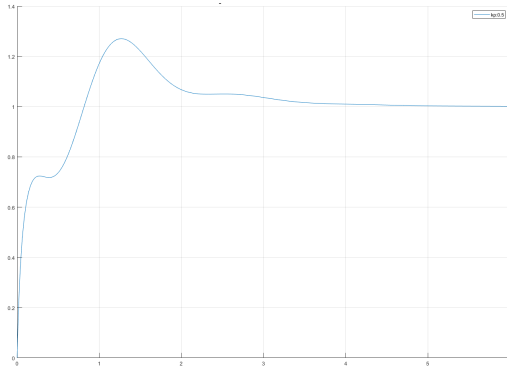

Figure 10: Step response (final gains)

The selected gains, as well as the proportional gain saturation limit, for lateral autopilot's inner loop, are presented in Table 8.

k_p	k_i	k_d	e_{max}	$\delta_{a_{max}}$	$k_{p_{sat}}$
0.5	0.35	0.03	15°	30°	2

Table 8: Selected gains ϕ loop

The final step response (Figure 10) has 27% of overshoot, it has 3.35 seconds of settling time, and 3.6rad/sec of bandwidth (-3dB).

Now, moving to the outer loop. It is possible to design it separately, by modeling the inner loop as a gain of 1 only if its bandwidth is at least 5 times lower than the inner one (ideally 10 times).

The outer loop frequency must be lower than 0.36 rad/s to meet the bandwidth constraints so the k_i upper limit is 0.13. The wanted damping is close to 1 so the proportional gain value must be close to 0.6. To follow these calculations in detail see the thesis related with this document.

The model is tested for different gain configurations. The step used for design is 35° of course angle. The the final step response for the selected gains is depicted in Figure 11.
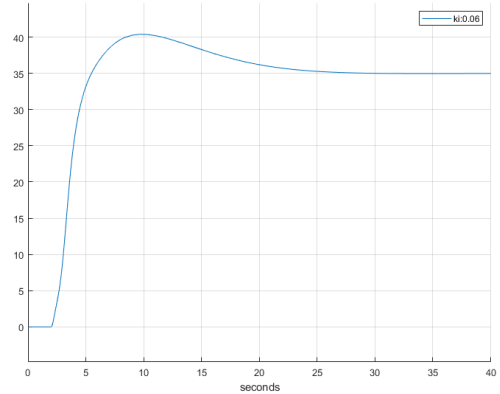

Figure 11: Step response, $k_p = 0.4$, $k_i = 0.06$.

The final response (Figure 11) is slower than the inner loop response. The overshoot is 14%, and the settling time is 22.1 seconds.

The longitudinal controllers are designed in the same way. The pitch inner loop has a static gain lower than one, the achieved θ does not converge to the desired one. The influence of k_d is small, especially for small proportional gains, but mitigates the first oscillation, which might be produced by the short period mode. The bandwidth increases as the k_p value raises, as well as the static gain, which approaches 0dB. Proportional gains over 1 yields a bandwidth of (-3dB) at 8 rad/s.

9

k_p	k_i	k_d	e_{max}	$\delta_{a_{max}}$	$k_{p_{sat}}$
0.8	0.6	0.03	10°	35°	3.5

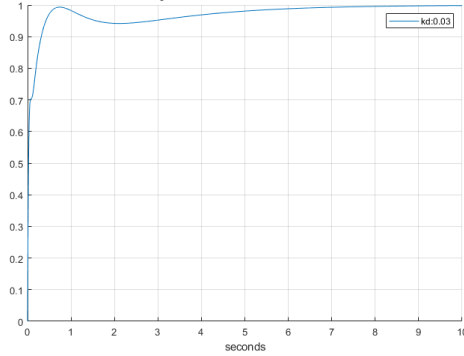Table 9: Selected gains θ loop for pitch hold mode.

Figure 12: Pitch response with final design gains.

In figure 12, the final response is presented. It is a fast, slightly under-damped response that tends to have small stationary errors. The selected gains for the outer loop that controls altitude are: $k_p = 0.3$ and $k_i = 0.015$. The target bandwidth frequency is 0.8 rad/s which gives an upper limit of 0.75 for the integrative gain.
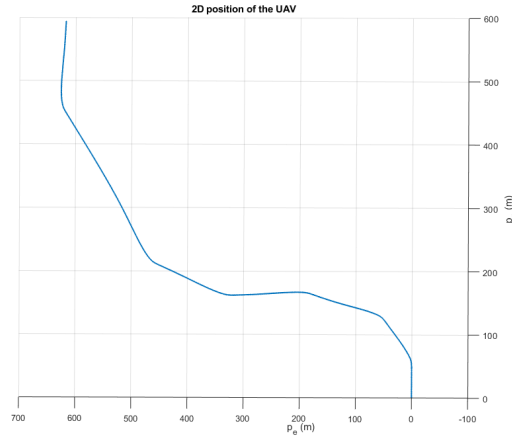

Figure 13: Autopilot test

In Figure 13, the autopilot is able to follow an established course pattern while it holds altitude as well, proving that the whole design is successful.

5. Conclusions

This work proves that it is possible to build low-cost UAV prototypes using inexpensive materials and determine the stability properties by selecting the most relevant dynamic features and designing tailor-made wind tunnel experiments.

The available open-source simulation software, $XFRL5$, is a good tool to do a first design step.

The stability issues of flying wings improve by combination of a better wing and control design.

References

[1] Alejandro Álvarez Monteagudo. Design and performance assessment of an adaptable small scale uav, September 2022.

[2] Faliang Wang. The comparison of aerodynamics and stability characteristics between conventional and blended wing body aircrafts, 2011/2012.

[3] Petterson Emil. Design of a drone system for maritime search and rescue missions, 2020.

[4] Martin Hepperle. Airfoils for tailless airplanes: Design and selection. https://www.mh-aerotools.de/airfoils/nf_2.htm, (visited on 06/10/2022)., 2018.

[5] Roberto Merino Martínez. Design and analysis of the control and stability of a blended wing body aircraft. Technical report, KTH, 2014.

[6] Wikipedia. Flying wing. https://en.wikipedia.org/wiki/Flying_wing, (last visit on 06/10/2022).

[7] Miguel Ángel Gómez Tierno, Manuel Pérez Cortés, and César Puentes Márquez. *Mecánica del vuelo*. Ibergaceta, 2012.

[8] Wikipedia. Perturbation theory. https://en.wikipedia.org/wiki/Perturbation_theory, (last visit on 06/10/2022).

[9] Wikipedia. Control theory. https://en.wikipedia.org/wiki/Control_theory, (last visit on 06/10/2022).

[10] Eduardo Núñez. Zyklon 400 : Flying wing protoype.

[11] João Luís Câmara Ornelas. Scaled uav prototyping and control., July 2021.

[12] NASA. Propeller thrust model based on bernoulli's principle. https://www.grc.nasa.gov/www/k-12/airplane/propth.html, (last visit on 06/10/2022).

[13] Randal W Beard and Timothy W McLain. *Small unmanned aircraft: Theory and practice.* Princeton university press, 2012.

[14] Wikipedia. Potential flow. https://en.wikipedia.org/wiki/Aerodynamic_potential-flow_code, (last visit on 06/10/2022).

[15] Oleh Tkachuk. Detailed design of a forest surveillance uav. Technical report, Tecnico Lisboa, 2018.